Orbital Order, Structural Transition and Superconductivity in Iron Pnictides

Yuki Yanagi [*], Youichi Yamakawa, Naoko Adachi and Yoshiaki Ōno

Department of Physics, Niigata University, Ikarashi, Niigata 950-2181, Japan

We investigate the 16-band d-p model for iron pnictide superconductors in the presence of the electron-phonon coupling g with the orthorhombic mode which is crucial for reproducing the recently observed ultrasonic softening. Within the RPA, we obtain the ferro-orbital order below T_Q which induces the tetragonal-orthorhombic structural transition at $T_s = T_Q$, together with the stripe-type antiferromagnetic order below T_N. Near the phase transitions, the system shows the s_{++}-wave superconductivity due to the orbital fluctuation for a large g case with $T_Q > T_N$, while the $s_{\pm}$-wave due to the magnetic fluctuation for a small g case with $T_Q \leq T_N$. The former case is consistent with the phase diagram of doped iron pnictides with $T_s > T_N$.

The recently discovered iron pnictide superconductors[1,2] RFePnO$_{1-x}$F$_x$ (R=Rare Earth, Pn=As, P) with a transition temperature T_c exceeding 50K have attracted much attention. The parent compounds with $x = 0$ show the tetragonal-orthorhombic structural transition at T_s and the stripe-type antiferromagnetic (AFM) transition at T_N. The carrier doping x suppresses both of the transition temperatures T_s and T_N and induces the superconductivity. In RFePnO$_{1-x}$F$_x$, T_s is always higher than T_N, while in Ba(Fe$_{1-x}$Co$_x$)$_2$As$_2$, the simultaneous first-order transition for nondoped case splits into two transitions with doping x where $T_s > T_N$.[3]

Theoretically, the s-wave pairing with sign change of the order parameter between the hole and electron Fermi surfaces (FSs), so called $s_{\pm}$-wave, mediated by the AFM fluctuation was proposed as a possible pairing state in the iron pnictides.[4-6] The $s_{\pm}$-wave state with a full superconducting gap seems to be consistent with most of the experiments.[7] As for the impurity effects, however, the small T_c-suppression against nonmagnetic impurities[8,9] is not consistent with the $s_{\pm}$-wave state where T_c is considered to rapidly decrease with the nonmagnetic impurities.[10] Therefore, the s-wave state without sign change of the order parameter, so called s_{++}-wave, mediated by the orbital fluctuation which is enhanced due to the effects of the inter-orbital Coulomb interaction was proposed on the basis of the one-dimensional two-band Hubbard model[11,12] and the two-dimensional 16-band d-p model.[13]

Remarkably, drastic softenings of the elastic constants have been observed in recent ultrasonic experiments.[14-16] As the elastic constant C_ε is given by the second derivative of the total energy w.r.t. the strain field ε and includes the contribution such as $-g_\eta^2\chi_\eta$ with the susceptibility χ_η for the electric operator $\hat{\eta}$ linearly coupled with the strain field as $g_\eta\hat{\eta}\varepsilon$, the enhancement of χ_η is responsible for the softening of C_ε. The detailed ultrasonic measurements[16] revealed that nondoped and underdoped Ba(Fe$_{1-x}$Co$_x$)$_2$As$_2$ shows drastic softenings of the elastic constants with decreasing T down to T_s
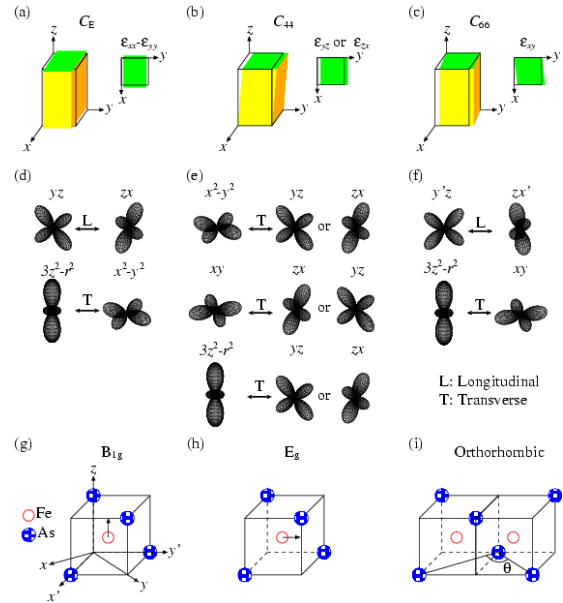

Fig. 1. (Color online) Schematic figures of the strain fields for C_E, C_{44} and C_{66} modes (a), (b) and (c), the orbital fluctuations coupled with the corresponding strain fields (d), (e) and (f), and the phonons for B_{1g}, E_g and orthorhombic modes which enhance the corresponding orbital fluctuations (g), (h) and (i), respectively. The x', y' (x, y) axes are directed along the nearest (second nearest) Fe-Fe bonds.

for $C_E = (C_{11} - C_{12})/2$, C_{44} and C_{66} modes relevant to the strain fields $\varepsilon_{xx} - \varepsilon_{yy}$, ε_{yz} (ε_{zx}) and ε_{xy} shown in Fig. 1 (a), (b) and (c) which are linearly coupled with the orbital fluctuations shown in Figs. 1 (d), (e) and (f), respectively, where x', y' (x, y) axes are directed along the nearest (second nearest) Fe-Fe bonds. The softening of C_{66} is much larger than C_E and C_{44} and exhibits divergent behavior when approaching a critical temperature T_Q which is just below T_s. Then, the orbital susceptibilities relevant to C_{66} mode, i. e., the longitudinal $d_{y'z}$-$d_{zx'}$ and/or transverse $d_{3z^2-r^2}$-d_{xy} shown in Fig. 1(f), are considered to diverge at T_Q below which the orbital order occurs and induces orthorhombic distortion via electron-lattice coupling resulting in the structural

*E-mail address: yanagi@phys.sc.niigata-u.ac.jp

transition at $T_s \sim T_Q$. In addition, optimally doped BaFe$_{1.84}$Co$_{0.16}$As$_2$ shows a significant softening of C_{66} mode down to T_c.[15] Therefore, the orbital order and its fluctuations relevant to C_{66} mode are considered to play crucial roles in both the structural transition and the superconductivity.

The orbital fluctuation is known to be enhanced by the electron-phonon interaction in addition to the inter-orbital Coulomb interaction. Recently, the effects of the electron-phonon interaction with B_{1g} and E_g modes on the orbital fluctuation and its induced s_{++}-wave super-conductivity have been investigated on the basis of the 5-band Hubbard model[17] and the 16-band d-p model.[18] As shown in Fig. 1, the B_{1g} phonon enhances the longitudinal d_{yz}-d_{zx} and transverse $d_{3z^2-r^2}$-$d_{x^2-y^2}$ orbital fluctuations responsible for the softening of C_E mode, while the E_g phonon enhances the transverse $d_{x^2-y^2}$-d_{yz}, d_{xy}-d_{zx} and $d_{3z^2-r^2}$-d_{yz} orbital fluctuations responsible for the softening of C_{44} mode. However, the effect of the orthorhombic mode which enhances the longitudinal $d_{y'z}$-$d_{zx'}$ and transverse $d_{3z^2-r^2}$-d_{xy} orbital fluctuations responsible for the most dominant softening of C_{66} mode was not considered there.[17, 18] The present paper is a straight-forward extension of our previous work[18] to include the orthorhombic mode which enable us to reproduce the ultrasonic softening of C_{66} and to obtain the x-T phase diagram including the tetragonal-orthorhombic structural transition and the superconductivity.

Our Hamiltonian of the two-dimensional 16-band d-p Holstein model, in which 3d orbitals ($d_{3z^2-r^2}$, $d_{x^2-y^2}$, d_{xy}, d_{yz}, d_{zx}) of two Fe atoms (Fe^1=A, Fe^2=B) and 4p orbitals (p_x, p_y, p_z) of two As atoms are explicitly included, is given by[18]

$$H = H_0 + H_{\text{int}} + H_{ph} + H_{el-ph}, \quad (1)$$

where H_0, H_{int}, H_{ph} and H_{el-ph} are the kinetic, Coulomb interaction, phonon and electron-phonon inter-action parts of the Hamiltonian, respectively. The kinetic part of the Hamiltonian H_0 includes the atomic energies and the transfer integrals which are determined so as to fit both the energy and the weights of orbitals for each band obtained from the tight-binding approximation to those from the density functional calculation for LaFeAsO and are listed in ref. 13. In the present model, the doping concentration x corresponds to the number of electrons per unit cell $n = 24 + 2x$ and there are two hole FSs (FS1 and FS2) around the Γ point and two electron FSs (FS3 and FS4) around the M point for $x = 0.1$. The Coulomb interaction part H_{int} includes the multi-orbital interaction on a Fe site: the intra- and inter-orbital direct terms U and U', Hund's rule coupling J and the pair transfer J'. For simplicity, we assume the relation $U = U' + 2J$ and $J = J'$ throughout this paper. Hereafter, we number the Fe-3d orbitals as follows: $d_{3z^2-r^2}(1)$, $d_{x^2-y^2}(2)$, $d_{xy}(3)$, $d_{yz}(4)$, $d_{zx}(5)$.

Now we consider the effect of the phonon and the electron-phonon interaction parts of the Hamiltonian H_{ph} and H_{el-ph} which includes the phonon energy ω_s and the electron-phonon coupling constant $g_s^{\ell\ell'}$ between the orbital ℓ and ℓ' (see Fig. 2 (a)), respectively, where
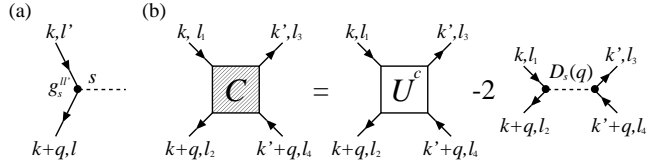

Fig. 2. Diagrammatic representation of the electron-phonon coupling $\hat{g}_s$ (a) and that of the bare vertex for the charge-orbital susceptibility $\hat{C}$ (b).

s represents the phonon mode. In the present paper, we consider the B_{1g}, E_g and orthorhombic modes as shown in Figs. 1 (g), (h) and (i). We note that the orthorhombic mode is not a normal coordinate but a general coordinate which is given by a linear combination of normal coordinates including both optical and acoustic modes. To avoid the difficulty with many phonon modes, we treat the orthorhombic mode as a local phonon similar to the B_{1g} and E_g modes as a simplest first step in including the orthorhombic mode. As following refs. 17 and 18, we take the electron-phonon coupling into account as the atomic energy variance of the Fe-3d electrons. The resulting electron-phonon coupling matrix elements are given as follows: $\sqrt{3}g_{E_g^1}^{15} = g_{E_g^1}^{25} = g_{E_g^1}^{34} = -\sqrt{3}g_{E_g^2}^{14} = g_{E_g^2}^{24} = -g_{E_g^2}^{35} = g_{E_g}$, $g_{B_{1g}}^{44} = -g_{B_{1g}}^{55} = \sqrt{3}/2 g_{B_{1g}}^{12} = g_{B_{1g}}$, $-\sqrt{3}/2 g_{\theta}^{13} = g_{\theta}^{45} = g_\theta$, $g_s^{\ell\ell'} = g_s^{\ell'\ell}$ and 0 for otherwise, where E_g^1 and E_g^2 correspond to the oscillation of the Fe atom along the x- and y-axis, respectively, and θ denotes the orthorhombic mode (see Fig. 1).

Within the RPA,[19] the spin susceptibility $\hat{\chi}^s(q)$ and the charge-orbital susceptibility $\hat{\chi}^c(q)$ are given in the 50×50 matrix representation as follows,[6, 13, 18]

$$\hat{\chi}^s(q) = [\hat{1} - \hat{\chi}^{(0)}(q)\hat{S}]^{-1}\hat{\chi}^{(0)}(q), \quad (2)$$

$$\hat{\chi}^c(q) = [\hat{1} + \hat{\chi}^{(0)}(q)\hat{C}]^{-1}\hat{\chi}^{(0)}(q) \quad (3)$$

with the noninteracting susceptibility, $\left[\hat{\chi}^{(0)}(q)\right]_{\ell_1\ell_2,\ell_3\ell_4}^{\alpha,\beta} = -(T/N)\sum_k G_{\ell_3\ell_1}^{\beta\alpha}(k)G_{\ell_2\ell_4}^{\alpha\beta}(k+q)$, where α, β $(=A, B)$ represent two Fe sites, ℓ represents Fe 3d orbitals, $\hat{G}(k) = [(i\varepsilon_n + \mu)\hat{1} - \hat{H}_0(\boldsymbol{k})]^{-1}$ is the noninteracting Fe-3d electron Green's function in the 10×10 matrix representation, μ is the chemical potential, $\hat{H}_0(\boldsymbol{k})$ is the kinetic part of the Hamiltonian with the momentum $\boldsymbol{k}$ given in eq. (1), $k = (\boldsymbol{k}, i\varepsilon_n)$, $q = (\boldsymbol{q}, i\nu_m)$ and $\varepsilon_n = (2n+1)\pi T$ and $\nu_m = 2m\pi T$ are the fermionic and bosonic Matsubara frequencies, respectively. It is noted that when the largest eigenvalue λ_{spin} (λ_{c-o}) of $\hat{\chi}^{(0)}(q)\hat{S}$ $(-\hat{\chi}^{(0)}(q)\hat{C})$ reaches unity, the magnetic (charge-orbital) instability occurs. In eqs. (2) and (3), bare vertices for the spin and charge-orbital susceptibilities $\hat{S}$ and $\hat{C}$ are given by[17, 18] $(\hat{S})_{\ell_1\ell_2,\ell_3\ell_4}^{\alpha,\beta} = (\hat{U}^s)_{\ell_1\ell_2,\ell_3\ell_4}^{\alpha,\beta}$, $(\hat{C})_{\ell_1\ell_2,\ell_3\ell_4}^{\alpha,\beta} = (\hat{U}^c)_{\ell_1\ell_2,\ell_3\ell_4}^{\alpha,\beta} - 2\delta_{\alpha\beta}\sum_s g_s^{\ell_2\ell_1}g_s^{\ell_3\ell_4}D_s(i\nu_m)$, where $D_s(i\nu_m) = 2\omega_s/(\nu_m^2 + \omega_s^2)$ is the local phonon Green's function for the mode s (see Fig. 2 (b)). The bare vertices due to the Coulomb interaction $\hat{U}^{s(c)}$ are given by, $(\hat{U}^{s(c)})_{\ell\ell,\ell\ell}^{\alpha\alpha} = U$ (U), $(\hat{U}^{s(c)})_{\ell\ell',\ell\ell'}^{\alpha\alpha} = U'$ ($-U'+2J$), $(\hat{U}^{s(c)})_{\ell\ell,\ell'\ell'}^{\alpha\alpha} = J$ ($2U'-J$) and $(\hat{U}^{s(c)})_{\ell\ell',\ell'\ell}^{\alpha\alpha} = J'$ (J'), where $\ell \neq \ell'$ and the other
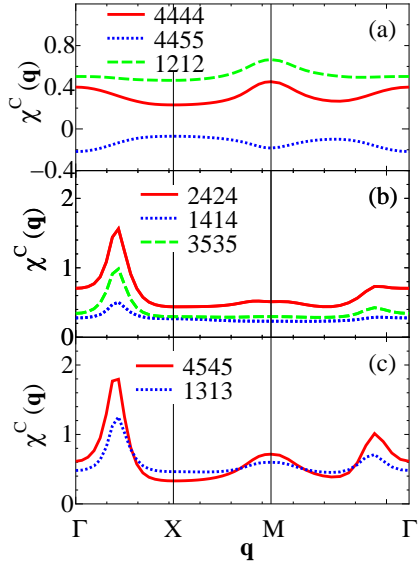
Fig. 3. (Color online) Several components of the charge-orbital susceptibility $\hat{\chi}^c(\boldsymbol{q}, 0)$ for $U' = 1.0$, $J = 0.2$ and $g = 0.065$ at $x = 0.1$ and $T = 0.036$, where we number the Fe-3d orbitals as follows: $d_{3z^2-r^2}(1)$, $d_{x^2-y^2}(2)$, $d_{xy}(3)$, $d_{yz}(4)$, $d_{zx}(5)$.

matrix elements are 0.

The linearized Eliashberg equation is given by

$$\lambda_{\text{sc}} \Delta_{\ell\ell'}^{\alpha\beta}(k) = -\frac{T}{N} \sum_{k'} \sum_{\ell_1 \ell_2 \ell_3 \ell_4} \sum_{\alpha',\beta'} V_{\ell\ell_1,\ell_2\ell'}^{\alpha,\beta}(k-k')$$

$$\times \ G_{\ell_3 \ell_1}^{\alpha'\alpha}(-k') \Delta_{\ell_3 \ell_4}^{\alpha'\beta'}(k') G_{\ell_4 \ell_2}^{\beta'\beta}(k'), \qquad (4)$$

where $\hat{\Delta}(k)$ is the gap function and $\hat{V}(q)$ is the effective pairing interaction for the spin-singlet state. Within the RPA, $\hat{V}(q)$ is given in the 50×50 matrix,

$$\hat{V}(q) = \frac{3}{2} \hat{S} \hat{\chi}^s(q) \hat{S} - \frac{1}{2} \hat{C} \hat{\chi}^c(q) \hat{C} + \frac{1}{2} \left(\hat{S} + \hat{C} \right). \quad (5)$$

The linearized Eliashberg equation (4) is solved to obtain the gap function $\hat{\Delta}(k)$ with the eigenvalue λ_{sc}. At $T = T_c$, the largest eigenvalue λ_{sc} becomes unity. We use 32×32 $\boldsymbol{k}$ point meshes and 512 Matsubara frequencies $(-511\pi T \leq \varepsilon_n \leq 511\pi T)$ in the numerical calculations for eqs. (2)-(5). For simplicity, we set $\omega_{B_{1g}} = \omega_{E_g^1} = \omega_{E_g^2} = \omega_\theta = \omega_0 = 0.02$eV as done in the previous study.[18] To reproduce the experimental results that the elastic softening is the largest for the C_{66} mode,[16] we assume $g_{B_{1g}} = g_{E_g} = 0.85 g_\theta$ and put $g_\theta = g$. Here and hereafter, we measure the energy in units of eV.

Fig. 3 shows several components of the static charge-orbital susceptibility $\hat{\chi}^c(\boldsymbol{q}, 0)$ for $U' = 1.0$, $J = 0.2$ and $g = 0.065$ at $x = 0.1$ and $T = 0.036$. In this case, the dimensionless electron-phonon coupling parameter is given by $\lambda = 2g^2\rho_0/\omega_0 \sim 2g^2/\omega_0 = 0.42$ with the density of states at the Fermi level $\rho_0 \sim 1/$eV. We find that, when T decreases, the transverse d_{yz}-d_{zx} orbital susceptibility $[\hat{\chi}^c(\boldsymbol{q}, 0)]_{45,45}^{A,A}$, which is equivalent to the longitudinal $d_{y'z}$-$d_{zx'}$ one, is most enhanced as compared to the other orbital and magnetic susceptibilities (not shown) due to the cooperative effects of the electron-phonon interac-
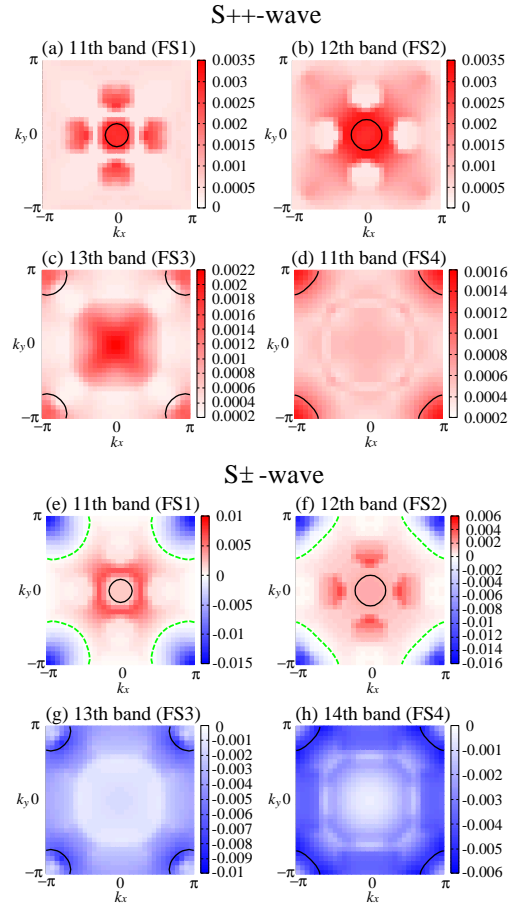

Fig. 4. (Color online) Several components of the gap function $\hat{\Delta}(\boldsymbol{k}, i\pi T)$ for $U' = 1.0$, $J = 0.2$ and $g = 0.065$ at $x = 0.1$ and $T = 0.036$ (a)-(d), and those for $U' = 1.48$, $J = 0.2$ and $g = 0.032$ at $x = 0.1$ and $T = 0.034$ (e)-(h).

tion with the orthorhombic mode and the inter-orbital Coulomb interaction U'.[13,18] We note that the incommensurate peaks around $\boldsymbol{q} = (0, 0)$ largely depend on the electron-phonon coupling strengths $g_s^{\ell\ell'}$ and move to the commensurate peak at $\boldsymbol{q} = (0, 0)$ for a slightly different parameter set where the resulting pairing state and the phase diagram discussed below is essentially unchanged.

In Figs. 4(a)-(d), we show several components of the gap function with the lowest Matsubara frequency $\hat{\Delta}(\boldsymbol{k}, i\pi T)$ obtained by solving the linearized Eliashberg equation (4) for the same parameters as in Fig. 3. In this case, the enhanced orbital susceptibility $\hat{\chi}^c(q)$ for $\boldsymbol{q} \sim (0, 0)$ (see Fig. 3), i. e., the ferro-orbital fluctuation yields the large negative value of the effective pairing interactions $\hat{V}(q)$ for $\boldsymbol{q} \sim (0, 0)$ due to the 2nd term of r.h.s. in eq. (5), resulting in the gap function without sign change, i. e., the s_{++}-wave state. For comparison, we also show the gap function in the case with a smaller (larger) value of g (U'), $U' = 1.44$, $J = 0.2$ and $g = 0.032$, in Figs. 4(e)-(h). In this case, the enhanced magnetic susceptibility $\hat{\chi}^s(q)$ for $\boldsymbol{q} \sim (\pi, \pi)$ (not shown), i. e., the stripe-type AFM fluctuation yields the large positive value of $\hat{V}(q)$ for $\boldsymbol{q} \sim (\pi, \pi)$ due to the 1st term of r.h.s. in eq. (5), resulting in the gap function with sign change, i. e., the $s_{\pm}$-wave state. We note that, the effects of the ferro-orbital
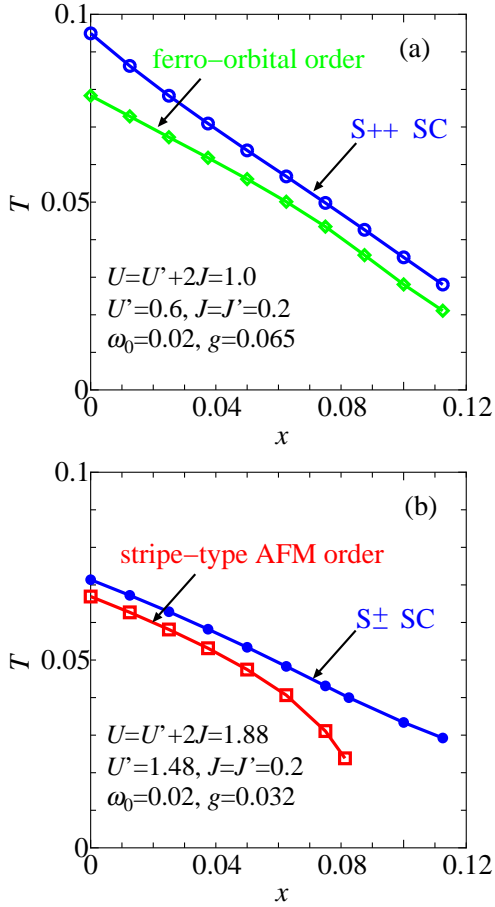
Fig. 5. (Color online) Phase diagram on the x-T plane for $U' = 1.0$, $J = 0.2$ and $g = 0.065$ (a) and that for $U' = 1.48$, $J = 0.2$ and $g = 0.032$ (b). The symbols represent the instabilities for the ferro-orbital order (diamonds), the stripe-type AFM order (squares), the s_{++}-wave superconductivity (open circles) and the $s_{\pm}$-wave superconductivity (closed circles), respectively.

and the AFM fluctuations on the superconductivity do not compete to each other as they are mainly responsible for the different $\boldsymbol{q}$ regions in $\hat{V}(q)$, in contrast to the case with the antiferro-orbital and the AFM fluctuations.

Fig. 5(a) shows the phase diagram on the x-T plane in the case with a large g, $U' = 1.0$, $J = 0.2$ and $g = 0.065$. When T decreases, the orbital susceptibilities $[\hat{\chi}^c(\boldsymbol{q}, 0)]^{A,A}_{45,45}$ and $[\hat{\chi}^c(\boldsymbol{q}, 0)]^{A,A}_{13,13}$ with $\boldsymbol{q} \sim (0,0)$ (see Fig. 3(c)) diverge at a critical temperature T_Q. Below T_Q, the ferro-orbital order with different occupations of the $d_{y'z}$ and $d_{zx'}$ orbitals occurs and induces the orthorhombic distortion resulting in the tetragonal-orthorhombic structural transition at $T_s = T_Q$. When approaching T_Q, the ferro-orbital fluctuation is largely enhanced and mediates the s_{++}-wave superconductivity (see Figs. 4(a)-(d)). We also investigate the same model within the Hartree-Fock approximation[20] and obtain the phase diagram consistent with RFePnO$_{1-x}$F$_x$ where $T_s = T_Q$ is always higher than the stripe-type AFM transition at T_N for the case with relatively larger (smaller) orbital (magnetic) fluctuation, and also obtain the phase diagram consistent with Ba(Fe$_{1-x}$Co$_x$)$_2$As$_2$ where the simultaneous first-order transition $T_s = T_Q = T_N$ for $x = 0$ splits

into two transitions $T_s = T_Q > T_N$ with doping x for a relatively smaller (larger) orbital (magnetic) fluctuation case. For the both cases, the ferro-orbital fluctuation dominates over the AFM fluctuation above $T_s = T_Q$ for $x > 0$ where the s_{++}-wave superconductivity is realized.

For comparison, we also show the x-T phase diagram in the case with a smaller (larger) value of g (U'), $U' = 1.44$, $J = 0.2$ and $g = 0.032$, in Fig. 5(b). When T decreases, the magnetic susceptibility with $\boldsymbol{q} \sim (\pi, \pi)$ diverges at T_N below which the stripe-type AFM order occurs and induces the ferro-orbital order[21] together with the orthorhombic distortion resulting in the tetragonal-orthorhombic structural transition at $T_s = T_N$, although the RPA result of T_Q is smaller than that of T_N. When approaching T_N, the AFM fluctuation is largely enhanced and mediates the $s_{\pm}$-wave superconductivity.[4–6] In this case, the simultaneous phase transition takes place at $T_s = T_N$ even for $x > 0$ and is inconsistent with the phase diagram of doped iron pnictides with $T_s > T_N$ which is reproduced for a large g case mentioned above.

In summary, we have shown that the ferro-orbital fluctuation relevant to the ultrasonic softening of C_{66} is enhanced by the electron-phonon coupling g with the orthorhombic mode and diverges at T_Q below which the ferro-orbital order with different occupations of the $d_{y'z}$ and $d_{zx'}$ orbitals occurs and induces the orthorhombic distortion resulting in the tetragonal-orthorhombic structural transition at $T_s = T_Q$. Near the transition, the s_{++}-wave superconductivity is realized due to the ferro-orbital fluctuation. The obtained x-T phase diagram is consistent with the phase diagram of doped iron pnictides with $T_s > T_N$, in contrast to a relatively small g case with $T_s = T_N$ where the $s_{\pm}$-wave superconductivity is realized due to the antiferromagnetic fluctuation. For both cases with s_{++}- and $s_{\pm}$-wave superconductivities, the RPA result of T_c is always higher than that of T_Q and/or T_N, where the orbital and/or the magnetic fluctuations diverge. With including the effects of the self-energy correction and the vertex correction neglected in the RPA, it is expected that the ferro-orbital order and/or the antiferromagnetic orders are realized for relatively small x, while the superconductivity is realized for relatively large x. The explicit caluculation including such effects is a future problem.

The obtained s_{++}-wave superconductivity seems to be consistent with experimental results of iron pnictides including the impurity effects. The enhanced ferro-orbital fluctuation above T_Q might be observed by experiments with a kind of external field inducing the anisotropy of x', y' axes, similar to the case with the ferromagnetic fluctuation above the Curie temperature observed by experiments with the external magnetic field. In fact, a resistivity anisotropy for $T > T_s$ is induced by uniaxial stress.[22] In the present paper, we treated the orthorhombic mode as a optical phonon, as a simplest first step. More realistic model including acoustic phonons together with a suitable parameter set of the electron-phonon coupling strengths $g_s^{ll'}$ will be discussed in a subsequent paper.

Acknowledgments

1) Y. Kamihara, H. Hiramatsu, M. Hirano, H. Y. R. Kawamura, T. Kamiya, and H. Hosono: J. Am. Chem. Soc. **128** (2006) 10012.
2) Y. Kamihara, T. Watanabe, M. Hirano, and H. Hosono: J. Am. Chem. Soc. **130** (2008) 3296.
3) D. K. Pratt, W. Tian, A. Kreyssig, J. L. Zarestky, S. Nandi, N. Ni, S. L. Bud'ko, P. C. Canfield, A. I. Goldman, and R. J. McQueeney: Phys. Rev. Lett. **103** (2009) 087001.
4) I. I. Mazin, D. J. Singh, M. D. Johannes, and M. H. Du: Phys. Rev. Lett. **101** (2008) 057003.
5) K. Kuroki, S. Onari, R. Arita, H. Usui, Y. Tanaka, H. Kontani, and H. Aoki: Phys. Rev. Lett. **101** (2008) 087004.
6) Y. Yanagi, Y. Yamakawa, and Y. Ōno: J. Phys. Soc. Jpn. **77** (2008) 123701.
7) D. C. Johnston: arXiv:1005.4392.
8) A. Kawabata, S. C. Lee, T. Moyoshi, Y. Kobayashi, and M. Sato: J. Phys. Soc. Jpn. **77** (2008) 103704.
9) M. Sato, Y. Kobayashi, S. Lee, H.Takahashi, E. Satomi, and Y. Miura: J. Phys. Soc. Jpn. **79** (2010) 014710.
10) S. Onari and H. Kontani: Phys. Rev. Lett. **103** (2009) 177001.
11) K. Sano and Y. Ōno: J. Phys. Soc. Jpn. **78** (2009) 124706.
12) M. Okumura, N. Nakai, H. Nakamura, N. Hayashi, S. Yamada, and M. Machida: Physica C **469** (2009) 932.
13) Y. Yanagi, Y. Yamakawa, and Y. Ōno: Phys. Rev. B **81** (2010) 054518.
14) M. A. McGuire, A. D. Christianson, A. S. Sefat, B. C. Sales, M. D. Lumsden, R. Jin, E. A. Payzant, D. Mandrus, Y. Luan, V. Keppens, V. Varadarajan, J. W. Brill, R. P. Hermann, M. T. Sougrati, F. Grandjean, and G. J. Long: Phys. Rev. B **78** (2008) 094517.
15) R. M. Fernandes, L. H. VanBebber, S. Bhattacharya, P. Chandra, V. Keppens, D. Mandrus, M. A. McGuire, B. C. Sales, A. S. Sefat, and J. Schmalian: arXiv:0911.3084.
16) M. Yoshizawa, R. Kamiya, R. Onodera, and Y. Nakanishi: arXiv: 1008.1479.
17) H. Kontani and S. Onari: Phys. Rev. Lett. **104** (2010) 157001.
18) Y. Yanagi, Y. Yamakawa, and Y. Ōno: Phys. Rev. B **82** (2010) 064518.
19) T. Takimoto, T. Hotta, and K. Ueda: Phys. Rev. B **69** (2004) 104504.
20) N. Adachi, Y. Yamakawa, Y. Yanagi, and Y. Ōno: presented at Autumn Meet. Physical Society of Japan (Sep. 2010), 25aWG-3.
21) K. Kubo, and P. Thalmeier: J. Phys. Soc. Jpn. **78** (2009) 083704.
22) J-H Chu, J. G. Analytis, K. D. Greve, P. L. McMahon, Z. Islam, Y. Yamamoto, and I. R. Fisher: Science **329** (2010) 824.